SYNTHESIS OF TERNARY AND QUATERNARY METAL OXIDES BASED ON Ni, Mn, Cu, AND Co FOR HIGH-PERFORMANCE SUPERCAPACITOR

M. KHAIRY[a, b, *], M. A. MOUSA[a]
[a]*Chemistry Departement, Benha University, Faculty of Science, Benha, Egypt*
[b]*Chemistry Department, College of Science, Imam Mohammad Ibn Saud lslamic University, Riyadh, KSA*

Mesoporous ternary oxides ($NiCo_2O_4$, $CuCo_2O_4$, $MnCo_2O_4$) and quaternary mixed oxides ($CuNiCo_2O_4$, $CuMnCo_2O_4$, $MnNiCo_2O_4$) are synthesized through a urea and surfactant-aided co-precipitation method, followed by a post-thermal treatment at 500 ºC. All materials are characterized by means of XRD, TEM-SAED, N_2-sorptiometry and FTIR spectrometry. All samples have a mesoporous structure. The $CuCo_2O_4$ sample consists of CuO (monoclinic) and $CuCo_2O_4$ spinel structure and $MnCo_2O_4$ consisted of α-MnO_2 and $MnCo_2O_4$ spinels structure. The supercapacitor performances of quaternary nano-oxides are examined in comparison with their corresponding ternary oxides by cyclic voltammetry (CV), charge-discharge (CD) and electrochemical impedance spectroscopy (EIS) measurements. Both $CuCo_2O_4$ and $MnCo_2O_4$ electrodes exhibit excellent supercapacitor performances that show a high specific capacitance of 915 F g^{-1} and 690 F g^{-1} at 56 mA g^{-1}, respectively. The quaternary mixed oxides have low performance. The $CuCo_2O_4$ and $MnCo_2O_4$ electrodes show capacitance retention of 99 and 98.8 %, respectively which explain their superior cycle stability.

1. Introduction

Energy storage and conversion have concerned enormous attention due to the growing need for electronic devices [1,2]. Recently, with the rising energy using up and the enlarged request for different energy origins, the imperative improvement of energy storage devices has attracted vast interest with respect to their nature of both high power density and desirable energy density. Recently, supercapacitors have been developed as attractive power sources with long lifetime and high charge/discharge rates [3]. Supercapacitors are attractive applicants for energy storage devices. But, the relatively poorer energy density than conventional batteries is the limitation of its more applications [4-6].

A supercapacitor can act as a bridge the gap between rechargeable batteries and electrolytic capacitors because of its high capacitance values which is much higher than other capacitors. Recently, a high energy storage capacity theoretically can be achieved at somewhat little cost by using the environment-friendly transition metal oxides which carry out greater redox activity and have a large natural abundance [7]. Recently, research has based on transition metal oxides and hydroxides, such as RuO_2, NiO, MnO_2, Co_3O_4, $Ni(OH)_2$ and $Co(OH)_2$ [8-13].

Today, the ternary metal oxides containing two unlike metal cations, typically have a high concern due to the hopeful roles in several fields such as using them in energy-related applications [14]. Many mixed oxides have various advantages such as achievable oxidation states, superb performances, high electrical conductivities, environmental friendliness, and low cost. $NiCo_2O_4$, $MnCo_2O_4$, and $MgCo_2O_4$ [15-17] etc. have been measured as potential, capable and scalable

---

* Corresponding author: mohkhairy@fsc.bu.edu.eg

alternatives [18]. Moreover, the micro-/nanostructures of oxides greatly affect the specific capacitance of the electrode materials.

The objective of the project is synthesizing a new nano-quaternary mixed oxides ($CuNiCo_2O_4$, $CuMnCo_2O_4$, $MnNiCo_2O_4$) and their comparative study with their nano-ternary oxides ($NiCo_2O_4$, $CuCo_2O_4$, $MnCo_2O_4$). The oxides were characterized by different techniques. The electrochemical properties of oxides were studied.

2. Experimental

2.1. Materials

All the chemical reagents used in the preparation were of A. R. grade and used without further purification and treatment. All materials: Cobalt nitrate ($Co(NO_3)_2 \cdot 6H2O$) (99 %), manganese sulphate ($MnSO_4 \cdot 2H_2O$) (99 %), nickel nitrate ($Ni(NO_3)_2 \cdot 6H_2O$) (99 %), copper nitrate ($Cu(NO_3)_2 \cdot 2H_2O$) (99 %), urea (99 %), ammonia (35 %) and sodium dodecyl sulphate (SDS) (98 %) were supplied from Aldrich.

2.2. Preparation methods
2.2.1. Preparation of ternary metal oxides

$NiCo_2O_4$ was prepared by the following procedure: stoichiometric amounts of nickel nitrate and cobalt nitrate, with 2:1 molar ratio of (Co: Ni), were dissolved in 150 ml of deionized water to produce an apparent pink solution, 10 mmol of urea in presence of 2×10^{-2} M SDS as template was then added, then the addition of 15 ml of 35 % ammonia solution with thirty minute magnetically stirring. The obtained reaction mixture was then preserved in the oven at 95 °C for 10 h. Pink precursors of $NiCo_2O_4$ were produced after cooling to room temperature, then washed several times with sufficient quantities of deionized ethanol and water. Thereafter, the precursors were dried at 80 °C overnight in an oven. Finally, the black $NiCo_2O_4$ nanoparticles were obtained, by annealing the precursors in an air atmosphere at 550 °C for 2 h with a heating rate of 5 °C/min.

The same procedures were performed to prepare $CuCo_2O_4$ and $MnCo_2O_4$ using copper nitrate, manganese sulphate, and cobalt nitrate.

2.1.2. Preparation of quaternary mixed metal oxides

$Cu_{0.5}Ni_{0.5}Co_2O_4$ was synthesized by the following procedures; stoichiometric amounts of $Ni(NO_3)_2 \cdot 6H_2O$, $Cu(NO_3) \cdot 2H_2O$ and $Co(NO_3)_2 \cdot 6H_2O$, with molar ratio of 0.5:0.5:2 (Ni: Cu: Co), were dissolved in 150 ml of deionized water to produce a clear pink solution, 10 mmol of urea in presence of 2×10^{-2} M SDS as template was then added, then addition of 15 ml of 35 % ammonia solution with 30 min. magnetically stirring. The reaction mixture obtained was then preserved in the oven for 10 h at 95 °C. Pink precursors of $CuNiCo_2O_4$ were produced after cooling to room temperature and then washed several times with sufficient quantities of deionized water and ethanol. Then, the precipitates were dried overnight at 80 °C in an oven. Finally, the black $CuNiCo_2O_4$ nanoparticles were obtained, by annealing the precursors in an air atmosphere at 550 °C for 2 h with a heating rate of 5 °C/min.

The same procedures were performed to prepare $MnNiCo_2O_4$ and $CuMnCo_2O_4$ using copper nitrate, manganese sulphate and cobalt nitrate.

2.2. Characterization tools

The crystalline phases for all investigated materials were recognized by X-ray diffraction (XRD) via a Diano (made in the U.S.A.). The patterns were run with Cu-filtered CuKα radiation ($\lambda = 1.5418$Å) energized at 45 kV, and 10 mA. The samples were measured in the range from 2θ $= 10$ to 80°. The phases present in the samples were known with the assist of ASTM Powder Data Files. The infrared spectra of the samples were measured via a KBr pellet on a Brucker-FTIR (Vector 22, made in Germany). High-resolution transmission electron microscopy (HRTEM) together with selected area electron diffraction (SAED) of the samples were used to investigate the morphologies of the samples as well as particle size via Tecnai G2- supper twin- USA. Nitrogen adsorption-desorption measurements were carried out by a Micromeritics ASAP 2020 surface area

and porosity analyzer. The samples were evacuated before the measurements for 1.0 hour at 363 K then 2 h at 473 K. The electrical conductivity and dielectric constant of the nanoxides were determined. The electrical measurements were performed at a constant voltage (1 volt) at room temperature at a frequency range from 100 Hz to 8 MHz by using a programmable automatic LCR bridge (model HIOKI IM 3536).

2.3. Electrochemical measurements

The electrochemical measurements of the prepared electrodes were studied to evaluate their capacitive parameters. The specific capacitance of the prepared samples was calculated depending upon the integrated area method via cyclic voltammetric (CV) curves. The galvanostatic charge-discharge technique (GCD) was used to calculate specific capacitance depending upon the discharge time method. Electrochemical impedance spectroscopy (EIS) was utilized to determine the different electrical parameters.

2.3.1. Preparation of working electrodes for supercapacitors

Electrodes were synthesized by mixing the studied material with carbon black and polyvinylidene fluoride (PVF) with percent ratio 80:10:5, respectively with few drops of ethanol to get slurry form, then assembling on (FTO), then dried at 180 °C for 2 h to vaporize solvent and achieve the best adhesion on the surface of the substrate.

2.3.2. Cyclic voltammetry (CV)

Capacitance was measured by cyclic voltammetry method in 2 M KCl electrolyte aqueous solution via (Digi-Ivy 2116 B), USA, in which the prepared materials were filmed on (FTO) glass, and stainless steel (SS). CV was carried out between the potential of (-1.1) to (+1) V with a triple system of prepared samples as working electrode vs. Saturated calomel electrode (SCE) as a reference electrode, while platinum electrode as a counter electrode at scan rates 10, 20, 50 and 100 mV/s.

2.3.3. Galvanostatic charge-discharge (GCD)

Galvanostatic charge-discharge (GCD) was employed to calculate the specific capacitance via chronopotentiometry through Digi-Ivy 2116 B-USA with DY2100B software for data calculation. The as-synthesized working electrodes were put in the electrochemical cell containing an electrolyte (2 M KCl) aqueous solution, with a triple system of prepared samples as working electrode vs. SCE and a platinum electrode. The synthesized working electrodes were evaluated at current densities of 56 and 105 mA g^{-1}.

2.3.4. Electrochemical impedance spectroscopy (EIS)

Electrochemical impedance spectroscopy (EIS) was measured with (Metrohm auto-lab PGSTAT 204), Netherlands. The prepared materials were filmed on (FTO), and (SS) electrodes, and measured in 2 M KCl aqueous solution with a triple system of prepared samples as working electrode vs. SCE as reference electrode, and Pt. E as counter electrode, in which the current ranged from 10 μA: 100 mA, frequency ranged from 0.1 Hz: 100 kHz and constant potential 10 mV.

3. Results and discussion

3.1. XRD and TEM investigations

Crystallographic structure of as-synthesized samples and products were characterized using X-ray diffraction (XRD). Fig. 1 shows the diffraction patterns of ternary metal oxides ($NiCo_2O_4$, $MnCo_2O_4$, and $CuCo_2O_4$) and quaternary mixed metal oxides ($MnNiCo_2O_4$, $CuMnCo_2O_4$, and $CuNiCo_2O_4$). The XRD patterns of $NiCo_2O_4$ (Fig. 1a) reveals that the peaks well match with the JCPDS card No. 20-0781) at $2\theta = 18.95°$, $31.2°$, $36.75°$, $38.42°$, $44.62°$, $55.56°$, $59.22°$ and $65.10°$, attributed to the (111), (220), (311), (222), (400), (422), (511) and (440) planes, respectively, characteristic to the spinel cubic structure of $NiCo_2O_4$.

The XRD pattern of $MnCo_2O_4$ material (Fig. 1 b) shows peaks at the values of 2θ at 18.45, 31.06, 36.36, 44.10, 58.73 and 64.48° indexed to (111), (220), (311), (400), (511) and (440) planes which agree can be well related to face centered-cubic (FCC) spinel $MnCo_2O_4$ with Fd-3m (227) space group (JCPDS card No. 023-1237, $\alpha=\beta=\gamma=90°$, a = b = c = 8.269 Å). In addition to this, there are two small peaks at 24.78 and 25.75° related to (220) and (112) indicating the presence of traces of α-MnO_2 (JCPDS Card No. 44-0141) and tetragonal Hausmannite Mn_3O_4 (JCPDS Card No. 75-1560).

The XRD of $CuCo_2O_4$ (Fig. 1f) shows diffraction peaks at 2θ values of 19.03°, 31.35°, 36.91°, 38.86°, 44.89°, 55.75°, 59.41° and 65.24° related to the (111), (220), (311), (222), (400), (422), (511) and (440) lattice planes, respectively, which were indexed as a cubic $CuCo_2O_4$ with a spinel structure with space group of Fd3m (JCPDS card no. 001- 1155) [19]. The pattern shows also peaks at 32.57°, 35.61°, 38.86°, 48.68°, 58.46°, 61.62°, and 68.21° correspond to the (110), (-111), (111), (-202), (202), (-113) and (220) lattice planes, respectively, indicating the formation of CuO (monoclinic phase) with a monoclinic structure (JCPDS No. 96-410-5686). This suggests formation $CuO/CuCo_2O_4$ composite. Further, the growth of the particle is oriented in a particular direction for $CuCo_2O_4$ phase which shows the high intensity plane (311) [20].
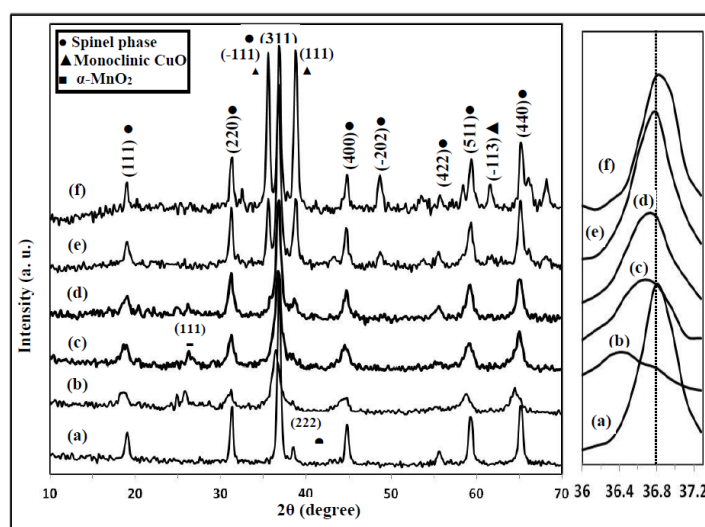

Fig. 1. XRD patterns of a) $NiCo_2O_4$ b) $MnCo_2O_4$ c) $MnNiCo_2O_4$ d) $CuMnCo_2O_4$ e) $CuNiCo_2O_4$ f) $CuCo_2O_4$.

On comparison of quaternary oxides namely $CuMnCo_2O_4$, $CuNiCo_2O_4$ with $CuCo_2O_4$, it was observed that for $CuNiCo_2O_4$ the cubic spinel structure phase was formed beside the peaks characteristic to CuO with a drastic decrease in their intensities which confirmed from the percentage of CuO phase. The percentage of the CuO phase is calculated from the high intensity CuO plane using the following equation [21]: Percentage of CuO = I_{CuO} / [I_{spinel} + I_{CuO}]

I_{CuO} and I_{spinel} are the maximum intensity of X-ray peaks of CuO and $CuCo_2O_4$, $CuNiCo_2O_4$ or $CuMnCo_2O_4$ spinels, respectively. The percentage calculated for CuO is 48, 29, 0 for $CuCo_2O_4$, $CuNiCo_2O_4$, and $CuMnCo_2O_4$, respectively. This indicates that the replacing nickel atoms with half of the copper atoms induce the introduction of Cu atoms in the formation of the spinel structure. On the other hand, for $CuMnCo_2O_4$ introducing Mn prevent the formation of CuO phase. Also, it can say that introducing the Cu into $MnCo_2O_4$ does not affect the spinle structure of $MnCo_2O_4$

On the other hand, The XRD pattern of $MnNiCo_2O_4$, quaternary metal oxide shows the formation of spinel structure with the presence of a very small peak at 26.2° indicating the presence of traces of Mn_3O_4. On comparison with $MnCo_2O_4$, it was observed that the replacement of Mn atoms with half Ni atoms, induce the disappearance of peaks at 24.8° and 25.7° of MnO_2 and appearing peak at 26.2° related to Mn_3O_4. But replacing Mn with Ni in $NiCo_2O_4$ don't affect

on the spinel structure in addition to inducing the presence of traces of Mn_3O_4. Along with, it is clear that there is a shift of the diffraction peaks of samples with each other which may be due to the differences of the metal ionic radii of Cu, Mn, and Ni. The inst Fig.1 shows the enlarged view of (311) lattice planes of $NiCo_2O_4$, $MnCo_2O_4$, $CuCo_2O_4$, $MnNiCo_2O_4$, $CuMnCo_2O_4$, and $CuNiCo_2O_4$. It shows that the 2θ values of diffraction peaks are about 36.75°, 36.36°, 36.91°, 36.78°, 36.79°, and 36.83°, respectively.

The lattice parameter values (a = b = c) of the $NiCo_2O_4$, $MnCo_2O_4$, $CuCo_2O_4$, $MnNiCo_2O_4$, $CuMnCo_2O_4$ and $CuNiCo_2O_4$ samples were calculated using the relation $1/d_{(hkl)}^2 = (h^2+k^2+l^2)/a^2$ are 8.11 Å, 8.19 Å and 8.07 Å, 8.099 Å and 8.096 Å and 8.09 Å, respectively. This variation in the lattice parameter values related to the difference in ionic radii of Mn^{+2} (0.97 Å), Ni^{+2} (0.83 Å) and Cu^{+2} (87 Å). The $CuCo_2O_4$ has larger than that of $NiCo_2O_4$ may be due to the presence of a new phase of CuO which affect the lattice parameter of spinel crystal. It is clear that the lattice parameter value of $MnNiCo_2O_4$ (8.099 Å) is less than both of $NiCo_2O_4$, and $MnCo_2O_4$ (8.11 Å, 8.19 Å) while The lattice parameter values of $CuMnCo_2O_4$ and $CuNiCo_2O_4$ samples lie in between their corresponding ternary metal oxides.

The average crystallite sizes of $NiCo_2O_4$, $MnCo_2O_4$, $CuCo_2O_4$, $MnNiCo_2O_4$, $CuMnCo_2O_4$, and $CuNiCo_2O_4$ samples are evaluated by Scherer's equation [22] using all diffraction peaks in the XRD patterns and given in Table 1. It was observed that the crystallite sizes of quaternary metal oxides are smaller than that of their corresponding ternary metal oxides.

Table 1. The average crystallite size from XRD, surface area, pore radius and pore volume of all investigated samples.

Samples	D_{XRD} (nm)	S_{BET} (m^2/g)	Pore radius (nm)	Pore volume (cc/g)
$NiCo_2O_4$	26	41	24.41	0.252
$MnCo_2O_4$	20	28	10.63	0.073
$CuCo_2O_4$	20.4	30	11.3	0.084
$CuNiCo_2O_4$	17	25	10.8	0.06
$CuMnCo_2O_4$	15	35	12.23	0.107
$MnNiCo_2O_4$	10	51	7.437	0.191

The morphologies of as-synthesized ternary and quaternary metal oxides were studied via TEM (Fig. 2). The TEM image of $NiCo_2O_4$ sample (Fig. 2 a) shows anisotropic shapes consists of spherical and plate-like particles with an average diameter of 13 nm in addition to rod shapes with the length of 61 nm and width of 12 nm. Fig. 2 (a) shows the HRTEM micrographs of the $NiCo_2O_4$ particles, with the lattice fringes of the selected area of particles. It shows that the inter-fringe distances of the particles are 0.48 nm and 0.20 nm, which agree well with the (111) and (400) planes of $NiCo_2O_4$, respectively, indicating the good crystallization of the nanoparticles. The corresponding SAED pattern of $NiCo_2O_4$ reveals definite sharp rings, characterizing $NiCo_2O_4$ nanocrystals via the exposed (111), (220), (311) (222), (400) and (422) planes in agreement with XRD results.
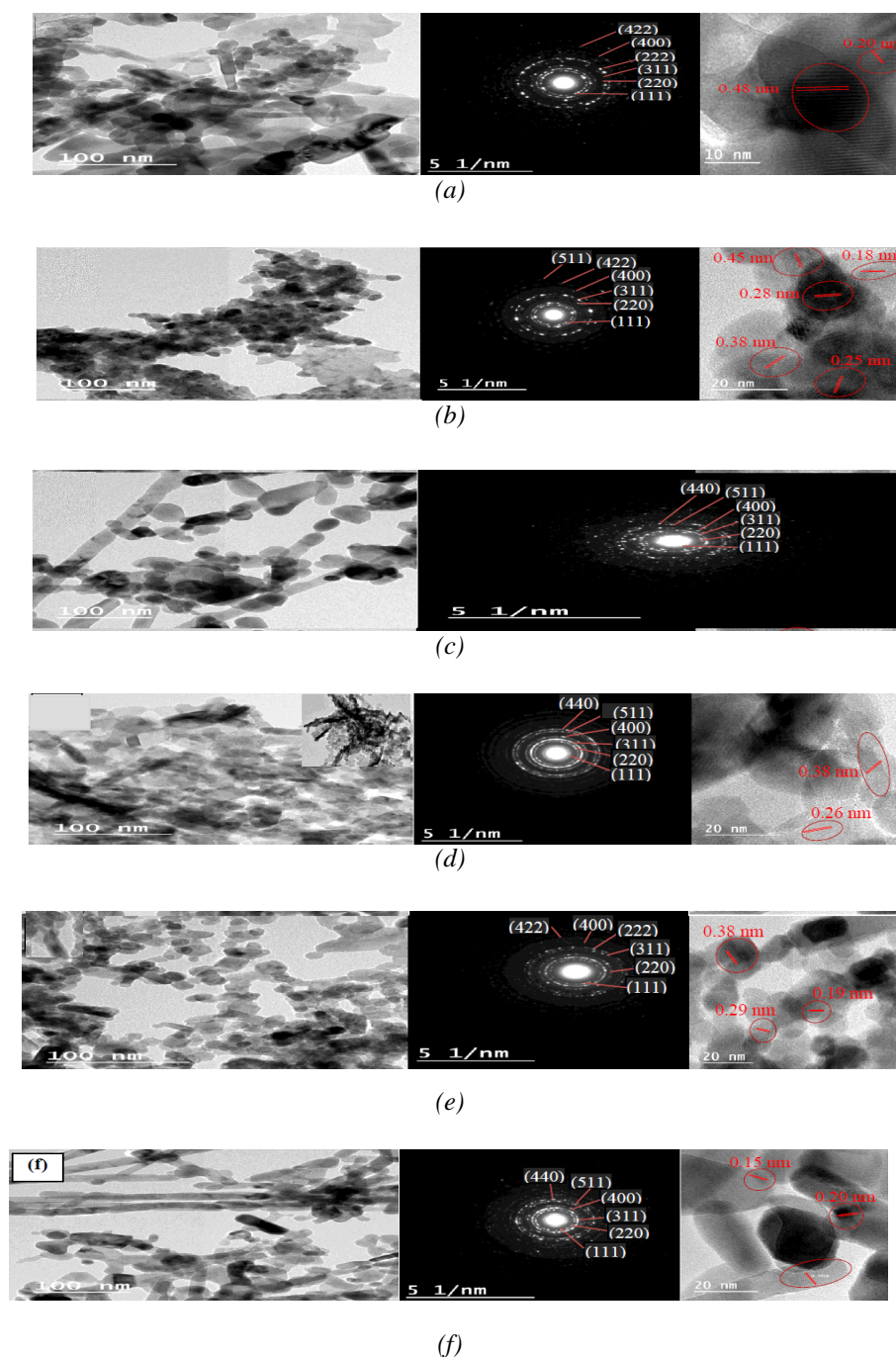
(a)

(b)

(c)

(d)

(e)

(f)

Fig. 2. TEM, HRTEM and SAED patterns of (a) $NiCo_2O_4$; (b) $MnCo_2O_4$; (c) $CuCo_2O_4$; (d) $MnNiCo_2O_4$; (e) $CuMnCo_2O_4$; (f) $CuNiCo_2O_4$.

The TEM image of $MnCo_2O_4$ revealed in Fig. 2 b shows the high homogeneous structure of nanospheres particles with an average diameter of 14 nm. The high-resolution TEM image (HRTEM) of the $MnCo_2O_4$ nanospheres. The lattice fringes are characteristics of the cubic spinel $MnCo_2O_4$, in which the d-spacing of 0.45 nm, 0.28 nm, 0.25 nm and 0.18 nm related to the distance of the (111), (220), (311) (222) and (400) planes, respectively, of the $MnCo_2O_4$ crystal in addition to the interplanar distance of 0.38 nm, which can be assigned to (220) plane of α-MnO_2 phase. Its corresponding SAED pattern suggests $MnCo_2O_4$ cubic spinel nanostructure via the existed planes (111), (220), (311), (400), (422) and (511); in agreement with XRD results.

The TEM images (Fig. 2 c) exhibit the morphology of $CuCo_2O_4$ sample. The TEM image reveals rod-like morphology with a very high aspect ratio with some aggregation of spherical

particles with a diameter of 11.5 nm which suggest the presence of CuO (black) connected with $CuCo_2O_4$ particles (light). The rods have an average length of 180 nm with a diameter of 26 nm. The sample shows irregular pores on the surfaces of these nanorods. The Fig. 2 c reveals the SAED pattern which can be well indexed to the spinel polycrystalline structure, in addition, the presence of a plane (111) of CuO.

The TEM image (Fig. 2 d) of $NiMnCo_2O_4$ sample reveals the two shapes of particles with rod shape with an average length of 60 nm and diameter of 7.5 nm, and spherical with a diameter of 8 nm. The Fig. 2d shows the SAED pattern which can be related to the spinel polycrystalline structure, in addition, the presence of plane (112) of Mn_3O_4 phase. The HRTEM shows also tow plane distance of 0.38 nm related to (222) plane of spinel structure and 0.26 nm related to (112) plane of Mn_3O_4 indicating the presence of traces of Mn_3O_4 as confirmed in XRD.

The TEM images (Fig. 2 d) show the morphology of $CuMnCo_2O_4$ sample. The micrograph shows homogeneous spherical particles with diameter 11.7 nm and some particles have rod structures with average length 45 nm and diameter 18.8 nm. The SEAD show pattern can be indexed to polycrystalline spinel structure and the HRTEM show different plane distances of 0.38 nm related to (220) plane of MnO_2 phase and at 0.29 nm and 0.19 nm which can be indexed to (220) and (400) planes, respectively, related to the spinel structure of $CuMnCo_2O_4$. This indicates the presences of traces of MnO_2 with spinel formed as confirmed by XRD.

The TEM images (Fig. 2 d) show the morphology of $CuNiCo_2O_4$ sample. The micrograph shows homogeneous rod particles with high aspect ratio with average length 142 nm and diameter 37.5 nm and some dispersed spherical particles with diameter 11.5 nm. The SEAD show pattern can be indexed to polycrystalline spinel structure and the HRTEM show different plane distances of 0.28 nm, 0.20 nm which can be indexed to (220), (400), respectively, related to the spinel structure of $CuMnCo_2O_4$ and 0.15 nm related to (202) plane of CuO phase This indicates the presences of traces of CuO with spinel formed as confirmed by XRD.

Generally, under the suitable thermal conditions urea was decomposed in aqueous solutions. The decomposition results in the production of NH^{4+} and OH^-, causing the increase of the pH of the medium. Earlier researches show that with moderate urea concentrations (5–10 mmol), the urea homogeneously and slowly generates the HCO_3^- and OH^- ions causing the precipitation of metal ions homogeneously into the metal hydroxycarbonate nanoparticles [23, 24]. Here, nanospheres were formed for the produced precipitate which then decayed to a spinel oxide structure after high thermal treatment (550 °C).

In general, for all samples, an Ostwald ripening is the growth mechanism of nanorods in which the nanorods develop at the expense smaller ones due to their various surface energies [25], and the splitting process (crystal nuclei aggregation/ particle ripening/lamellar structure splitting) to nanorods [26–29].

The surfactant also has an effective role in the growth process. The SDS surfactant accelerates the reaction of the growth units beside facilities their oriented growth [30]. SDS ionizes completely in water to SDS- with negatively charged head and a long hydrophobic tail which can interact with the formed precursors via electrostatic interaction. This leads to the oriented growth of the metal hydroxycarbonate or metal hydroxide resulted in the formation of nanorods.

3.2. Surface texturing properties

The surface texturing of the synthesised ternary metal oxides ($NiCo_2O_4$, $MnCo_2O_4$, $CuCo_2O_4$) and quaternary metal oxides ($MnNiCo_2O_4$, $CuMnCo_2O_4$, $CuNiCo_2O_4$) nanocomposites is studied by the N_2 adsorption/desorption isotherm, as shown in Fig. 3, where the inset is the pore size distribution plots determined according to the Barrett-Joyner-Halenda (BJH) analysis. The isotherms show typical type IV with H_3 type hysteresis loop, based on IUPAC classification [31]. These isotherms suggest the mesoporous structure of all samples and characterizing aggregates of plate-like or slit-shaped pores [32-33].
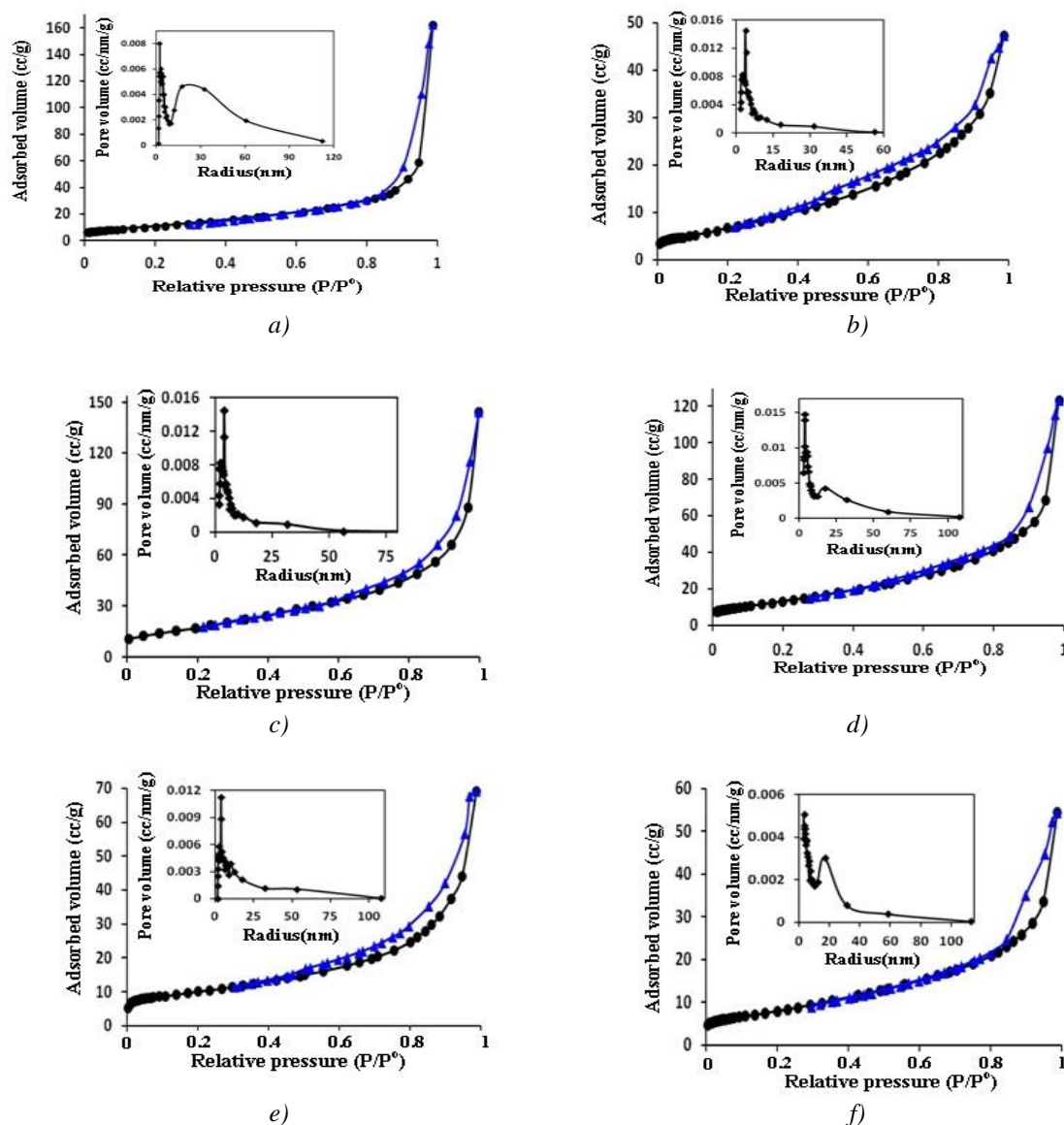
Fig. 3. Adsorption-desorption isotherms and pore size distribution curves (inset) of
a) NiCo$_2$O$_4$ b) MnCo$_2$O$_4$ c) CuCo$_2$O$_4$ d) MnNiCo$_2$O$_4$ e) CuMnCo$_2$O$_4$, and f) CuNiCo$_2$O$_4$.

It was found that the nitrogen adsorption-desorption isotherms shape is strongly affected by the composition of the different oxides. The hysteresis loops of the samples close at different P/P^o values of 0.84, 0.36, 0.85, 0.52, 0.46 and 0.64 for NiCo$_2$O$_4$, MnCo$_2$O$_4$, CuCo$_2$O$_4$, MnNiCo$_2$O$_4$, CuMnCo$_2$O$_4$, and CuNiCo$_2$O$_4$ nanooxides, respectively. These suggest the presence of larger pores in NiCo$_2$O$_4$ and CuCo$_2$O$_4$ samples compared to the rest samples. The lowest P/P^o value (0.36) at which the hysteresis loop closes was for the sample MnCo$_2$O$_4$ suggesting pore narrowing of this sample, comparatively [34]. The BET analysis (Table 1) exposed that the surface area was in the order: MnNiCo$_2$O$_4$ > NiCo$_2$O$_4$ > CuMnCo$_2$O$_4$ > CuNiCo$_2$O$_4$ > CuCo$_2$O$_4$ > MnCo$_2$O$_4$. It was found that the sample MnNiCo$_2$O$_4$ of the lowest particle size has the largest surface area (51.4 m^2/g). It was found that both ternary oxides MnCo$_2$O$_4$ and CuCo$_2$O$_4$ display low surface areas (28 and 30 m^2/g, respectively) besides CuNiCo$_2$O$_4$ (25 m^2/g). This may be attributed to the presence of CuO phase in both CuCo$_2$O$_4$ and CuNiCo$_2$O$_4$.

Table 1 shows that the pore radius of all samples indicating the mesoporosity structure of all samples. The pore-size distribution (PSD) for NiCo$_2$O$_4$ signifies that it is consists of a bimodal type of pore of mesoporosity centered at 24 Å together with a broad one 175 Å. The PSD obtained

for both $MnCo_2O_4$ and $CuNiCo_2O_4$ revealed a pore with monomodal type maximized at 37 Å and 36 Å. $CuCo_2O_4$ illustrated a pore with a bimodal distribution centered at 31 Å together with a broad one centered at 170 Å. $MnNiCo_2O_4$ showed a bimodal distribution centered at 39 Å; as a shoulder, together with a broad one centered at 172 Å. $CuMnCo_2O_4$ exhibited a trimodal distribution centered at 39 Å and two as a shoulder at 73 and 99 Å as a shoulder. The pore volume of both $NiCo_2O_4$ and $MnNiCo_2O_4$ samples is larger than that of the other samples (0.252, 0.191 cm^3/g, respectively).

3.3. FTIR spectroscopy

The FTIR spectra of all investigated samples were displayed in Fig. 4. The FTIR spectrum of $NiCo_2O_4$ (Fig. 4 a) shows several absorption bands at 3406, 2923, 1604, 1037, 658, 562 cm^{-1}, respectively. Two strong absorption bands at 658 cm^{-1} and 562 cm^{-1} related to the metal-oxygen stretching in both tetrahedral and octahedral sites, respectively. These are the characteristics of cobaltites [35]. The band at 1604 cm^{-1} is assigned to the angular deformation of absorbed water molecules. A small band at 2923 cm^{-1} is due to the νC–H stretching vibrations [36]. The band at 3407 cm^{-1} is related to the coordinated or entrapped water in the sample. The band at 1048 cm^{-1} corresponds to the bending vibrations of OH groups [37].

The FTIR spectrum of $MnCo_2O_4$ (Fig. 4b) displays absorption bands at 3381, 1624, 1132, 852, 651, 553 cm^{-1}, respectively. The band at 3381 cm^{-1} was related to the stretching vibration of OH groups, while the bands at 1624, and 1132 cm^{-1} related to the OH bending vibrations [37]. Two sharp bands appear at 553 and 651 cm^{-1} related to the metal– oxygen bond stretching vibration. These two bands attributed to the vibration of cobalt or manganese ions in the octahedral site and the tetrahedral site in the spinel lattice [38]. This result confirms the spinel structure formation, matched with the XRD data. The band at 1624 cm^{-1} is related to the bending vibration of absorbed water molecules.

The FTIR spectrum of synthesized $CuCo_2O_4$ (Fig. 4c) shows tow bands at 663 and 556 cm^{-1} related to the stretching vibration of Co^{3+} - O^{2-} in the octahedral sites and Cu^{2+}-O^{2-} at the tetrahedral sites, respectively indicating the presence of spinel $CuCo_2O_4$ [39]. However, the presence of a secondary phase, CuO does not reveal any change in the absorption band which confirms the occupation of the tetrahedral and octahedral sites with Cu^{2+} ions and Co^{3+}, respectively. Further, the appearance of broadband about 3412 cm^{-1} are attributed to both ν_{as}(O-H) and ν_s(O-H) [40]. Moreover, the bands at 1608 and 1116 cm^{-1} are attributed to the bending vibration ν(H-O-H) of hydrated water [41].

On the other hand, FTIR spectra of quaternary oxides are given in Fig. 4d-f. The FTIR spectrum of $NiMnCo_2O_4$ (Fig. 4d) shows several absorption bands at 3403, 1615, 1121, 866, 652, 557 cm^{-1}, respectively. The band at 3403 cm^{-1} was related to the OH stretching vibration, and the bands at 1615, and 1121 cm^{-1} assigned to the bending vibrations of OH groups [37]. Two sharp bands occur at 557 and 652 cm^{-1} due to the metal– oxygen bond stretching vibration. It was found that the wavenumber of these two bands is in between the values of the corresponding ternary oxides ($NiCo_2O_4$ and $MnCo_2O_4$) which indicates the effect of the presence of both Ni and Mn ions in the spinel structure. This may be attributed to the difference in lattice constant and cation distribution.
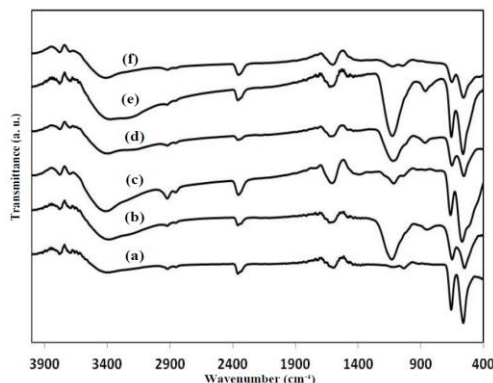
Fig. 4. FTIR spectra of a) NiCo$_2$O$_4$ b) MnCo$_2$O$_4$ c) CuCo$_2$O$_4$ d) MnNiCo$_2$O$_4$ e) CuMnCo$_2$O$_4$
f) CuNiCo$_2$O$_4$.

The FTIR spectrum of CuMnCo$_2$O$_4$ (Fig. 4e) reveals absorption bands can be observed at 3379, 1622, 1128, 864, 657, 564 cm^{-1}, respectively. The band at 3379 cm^{-1} was related to the stretching vibration OH groups, and the bands at 1622, and 1128 cm^{-1} attributed to the OH bending vibrations [37]. Two sharp bands occur at 564 and 657 cm^{-1} due to the stretching vibration of the metal– oxygen bond. These two bands are shifted compared to that in the corresponding ternary oxides (CuCo$_2$O$_4$ and MnCo$_2$O$_4$) indicating the effect of the presence of both Cu and Mn ions in the spinel structure.

The FTIR spectrum of CuNiCo$_2$O$_4$ (Fig. 4 f) shows absorption bands at 3413, 1604, 1124, 653, 560 cm^{-1}, respectively. The band at 3413 cm^{-1} was related to the stretching vibration of OH groups, and the bands at 1604, and 1124 cm^{-1} related to the bending vibrations of OH groups [37]. Two sharp bands occur at 560 and 653 cm^{-1} due to the stretching vibration of the metal– oxygen bond.

From all results the vibration wavenumbers of metal-oxygen bond in tetrahedral site and octahedral site lie in ranges 553-572 cm^{-1} and 651-663 cm^{-1}, respectively indicating the formation of spinel structure of all samples. It is clear that for ternary oxides (NiCo$_2$O$_4$, MnCo$_2$O$_4$ and CuCo$_2$O$_4$) the wavenumbers of v_{tetra} and v_{octa} decrease in the order CuCo$_2$O$_4$ > NiCo$_2$O$_4$ > MnCo$_2$O$_4$ which is matching with the order of increasing the lattice parameters of these samples as confirmed from XRD (CuCo$_2$O$_4$ < NiCo$_2$O$_4$ < MnCo$_2$O$_4$). On the other hand, the vibration wavenumbers of quaternary oxide samples lie in between the values of the corresponding ternary metal oxides in matching with XRD data. It is clear that the lattice parameter value of MnNiCo$_2$O$_4$ (8.099 Å) is less than both of NiCo$_2$O$_4$, and MnCo$_2$O$_4$ (8.11 Å, 8.19 Å) while The lattice parameter values of CuMnCo$_2$O$_4$ and CuNiCo$_2$O$_4$ samples lie in between the corresponding binary metal oxides. All shifts in all peaks based on the variation of structure, different ionic radii of different metals which affect their force constants as well as the different cation distribution of all samples.

3.4. Supercapacitive characteristics

The capacitive behavior of the electrode material can be investigated via cyclic voltammetry (CV). Fig. 5 reveal the CV curves of ternary and quaternary oxides measured in the potential window of -1.1 – 1V; performed in 2 M KCl, at a scan rate of 10 mVs^{-1} (enlargement of CV of NiCo$_2$O$_4$ is shown in inset Fig. 5). As shown for NiCo$_2$O$_4$, a couple of oxidation-reduction peaks are appeared for the electrode indicating the Faradaic capacitive behaviour, which is chiefly attributed to the reversible redox reaction of Ni^{2+}↔ Ni^{3+}and M^{3+}↔ M^{4+}transitions (M are indicative of Ni and Co) [42]. The asymmetric CV curves with redox reaction peaks indicate the Faradic pseudocapacitive behavior from oxides.

The non-rectangular behavior shown in the CV curves (Fig. 5) is the proof for the presence of redox reaction in CuCo$_2$O$_4$/CuO, between the active species of Co^{4+}/Co^{3+}. This suggests that the faradaic reaction happens at the surface of the electrode is the charge storage mechanism [43-45].

The CV curve of MnCo$_2$O$_4$ (Fig. 5) shows pairs of redox peaks consistent with the previous reports by Wang et al. indicating the pseudocapacitance behavior of it. The redox peaks related to the Mn^{2+}/Mn^{3+} and Co^{2+}/Co^{3+} redox reactions [46]. Due to the similar redox potentials of Co and Mn ions, it is difficult to inform them apart in the CV graph from the dissimilar peaks

associated with manganese and cobalt [47]. The deviation from the ideal rectangular shape and existence of a redox peak indicate a typical redox behavior of the electrode.
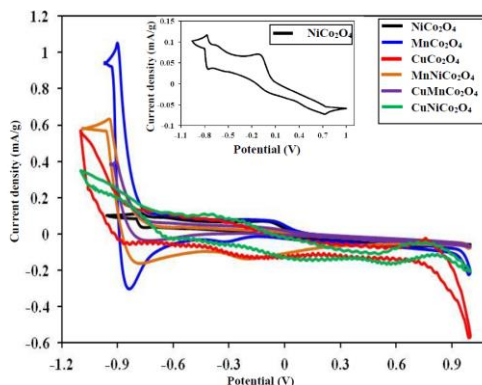

Fig. 5. The CV curves of all invesitegated samples measured in the potential window of -1.1:1V; performed in 2 M KCl, and at scan rate of 10 mV s^{-1}. Inset Fig. relates the enlargement of CV curve of NiCo$_2$O$_4$.

On the other hand, The CV curves of quaternary metal oxides show pairs of redox peaks indicate the materials also have a pseudocapacitance behavior. It was observed that the CV curve of CuNiCo$_2$O$_4$ has a similar shape to CuCo$_2$O$_4$ and NiCo$_2$O$_4$. While the CV curves of both NiMnCo$_2$O$_4$ and CuMnCo$_2$O$_4$ materials have the same shape as the MnCo$_2$O$_4$ with some deviations of the peaks for quaternary oxides.

By measuring the CV of the electrodes at different scan rates ranging between 10 and 100 mVs^{-1}, an increase in the current is observed with almost no significant change in the shapes of CV curves, as shown in Fig. 6. This refers to the high electron conduction within the electrode, and small equivalent series resistance [48]. on the other hand, the anodic peaks move towards more positive and the cathodic peaks to more negative potentials, by increasing the scan rates, which related to the quasi-reversible or non-reversible redox reactions, which are activated by the transfer of electron that involves association, isomerization, and dissociation reactions [49]. This irreversibility of the redox reactions, as shown by the asymmetric character of the CV curve, is due to the provoked polarization, ohmic resistance and the diffusion of the electrolyte in the porous electrode. These properties of the CV curve confirm the pseudocapacitance behavior of the all ternary and quaternary oxides.
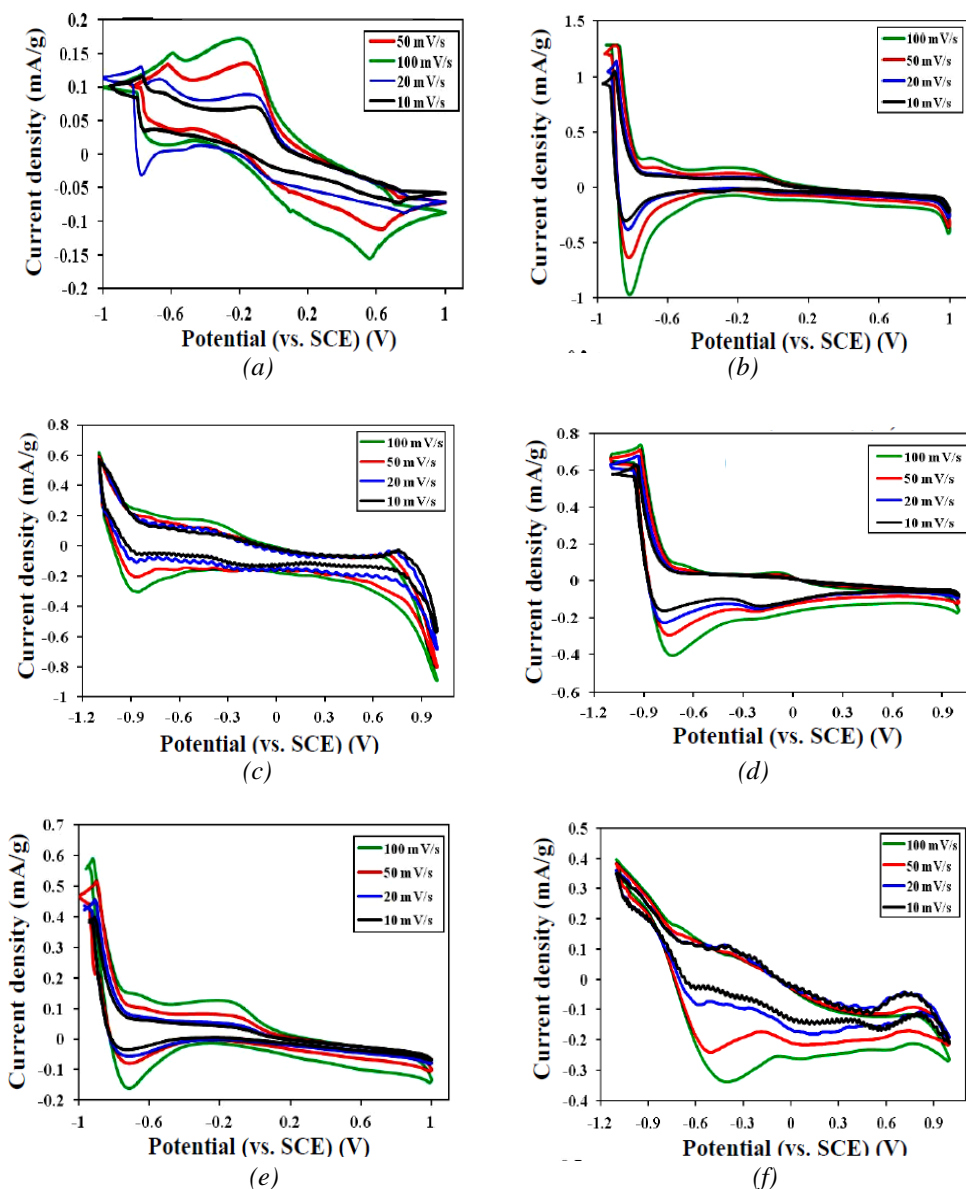
192

Fig. 6. The CV curves of a) NiCo$_2$O$_4$, b) MnCo$_2$O$_4$, c) CuCo$_2$O$_4$, d) MnNiCo$_2$O$_4$, e) CuMnCo$_2$O$_4$ and f) CuNiCo$_2$O$_4$ measured in the potential window of -1.1:1V; performed in 2 M KCl at the scan rates of 10, 20, 50 and 100 mV s^{-1}.

Our results also showed the specific capacitance decreased with raising the scan rate as shown in Fig. 6. The maximum values of all samples were attained at the scan rate of 10 mV s^{-1}. The existence of the porous rod structure of the active material may facilitate the diffusion of the electrolyte ions into the electrode and facilitates the diffusion-controlled faradaic reactions.

The electrochemical performances of the electrode materials were also examined by galvanostatic charge/discharge measurements. Fig. 7 shows the potential vs. time curves for ternary and quaternary oxides at 56 mA g^{-1}. The voltage plateau was detected in the charge and discharge curves of each sample, which agrees well the peaks exhibited in the CV curve and verifies the pseudocapacitance behavior of the materials.
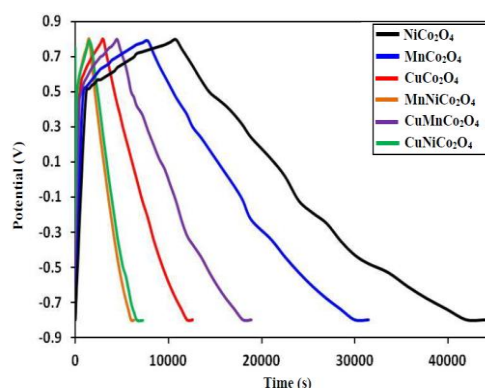
Fig. 7. The GCD curves for $NiCo_2O_4$, $MnCo_2O_4$, $CuCo_2O_4$, $MnNiCo_2O_4$, $CuMnCo_2O_4$ and $CuNiCo_2O_4$ performed in 2 M KCl at a current density 56 mA g^{-1}.

The deviation (distorted) appeared in the charge-discharge curves are attributed to the faradaic reaction (Pseudocapacitance), which is matched with the reported CV curves [50]. The specific capacitances of the studied electrodes were calculated using the discharge cycles via the following equation [51]:

$$C_{sp} = It/mV \qquad (2)$$

where I is the current loading (A), m is the mass of the active material in working electrode (g), V is the potential window (V) and t is the discharge time (s). The results show that the specific capacitances calculated at a current density of 56 mAg^{-1}, of the $CuCo_2O_4$, $NiCo_2O_4$, $MnCo_2O_4$, $MnNiCo_2O_4$, $CuMnCo_2O_4$, and $CuNiCo_2O_4$ are found to be 915, 390, 690, 147, 285 and 135 F g^{-1}, respectively, and given in Table 2. The values that obtained refer to that $CuCo_2O_4$ and $MnCo_2O_4$ samples exhibit the highest capacitance. The superior performance indicates $CuCo_2O_4$ with heterojunction of CuO with $CuCo_2O_4$ can suggest extra active sites and result in fast transmission of electrons and ions [52]. The high capacitance value of $CuCo_2O_4$ and $MnCo_2O_4$ may also due to the high dielectric constant and low conductivity of these samples compared to the other (Fig. 8). Rate capability is a significant factor for using the supercapacitor in power applications. Therefore, we studied the charge/discharge behavior of the investigated electrodes at different current densities (56 - 105 mA g^{-1}). Fig. 9 shows the equivalent specific capacitive at various current densities. Generally, the specific capacitance values increase as the current density decreases, which are attributed to the fact that the increasing voltage drop and some inner active materials cannot perform the redox transitions completely at higher current densities [53]. Indeed, decreasing the capacitance values by increasing the current density confirms the aforementioned CVs results in which an increase in capacitance was achieved as a function of the scan rate.
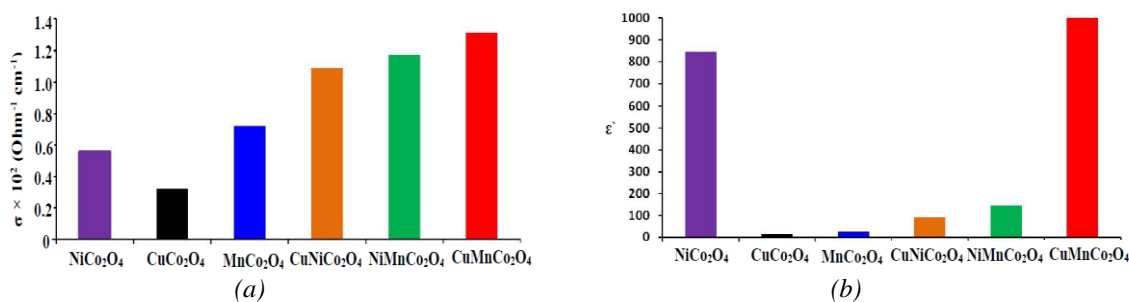

(a)

(b)

Fig. 8. (a) The electrical conductivity of $NiCo_2O_4$, $MnCo_2O_4$, $CuCo_2O_4$, $MnNiCo_2O_4$ and $CuNiCo_2O_4$; (b) The dielectric constant of $NiCo_2O_4$, $MnCo_2O_4$, $CuCo_2O_4$, $MnNiCo_2O_4$, $CuMnCo_2O_4$ and $CuNiCo_2O_4$.

Fig. 9. The specific capacitance values of $NiCo_2O_4$, $MnCo_2O_4$, $CuCo_2O_4$, $MnNiCo_2O_4$, $CuMnCo_2O_4$ and $CuNiCo_2O_4$ nano-oxides delivered using galvanostatic charge-discharge as a function of the current density (56 and 105 mA g^{-1}).

Table 2. Specific capacitance values evaluated from GCD plots at current density 56 mA g^{-1}, equivalent series resistance (R_s) and charge transfer resistance (R_{CT}) evaluated from EIS results of synthesized samples.

Sample	C_{sp} by GCD (F g^{-1})	R_s (Ω)	R_{CT} (Ω)
$CuCo_2O_4$	915	30	25
$NiCo_2O_4$	390	39	193
$MnCo_2O_4$	690	31	97
$MnNiCo_2O_4$	147	76	705
$CuMnCo_2O_4$	285	51	480
$CuNiCo_2O_4$	135	118	1900

Electrochemical stability of all electrode materials is tested by the charge-discharge measurements at the constant current density of 56 mA g^{-1} and shown in Fig. 10. The specific capacity of all electrodes material is well- preserved after cycling for 250 cycles. The specific capacitance remains after the 250 cycles for $CuCo_2O_4$, $NiCo_2O_4$, $MnCo_2O_4$, $MnNiCo_2O_4$, $CuMnCo_2O_4$ and $CuNiCo_2O_4$ by 99%, 86.5%, 97.8%, 62.5%, 98.4%, and 72.7%, respectively. It was found that $CuCo_2O_4$ sample has the highest retention ratio. The decreasing in the specific capacitance of other samples with cycle numbers may be ascribed to the metal-ions micro-granular dissolution and the PVDF (binder) in the electrolyte solution [54]

These data prove that the synthesized $CuCo_2O_4$ and $MnCo_2O_4$ samples due to their capability to produce a sufficient quantity of power and sustain a large specific capacitance value can act as a hopeful electrode material for supercapacitors.
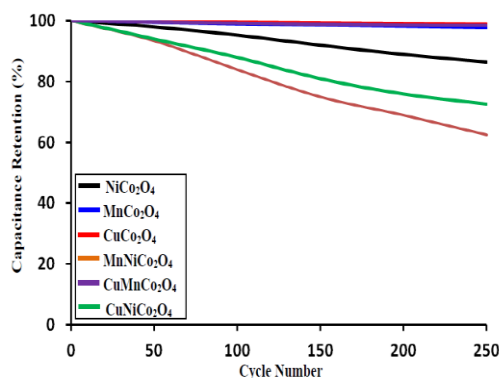
Fig. 10. Cycling performance of studied samples at a current density of 56 A g^{-1}.

Rate capability is a central aspect of the use of super-capacitors in power applications. A suitable electrochemical energy storage device is needed to deliver high energy density at a high charge/discharge rate. The energy density (E, Wh kg^{-1}) and power density (P, Wk g^{-1}) are two decisive factors for practical applications, therefore, they were evaluated using the following equations and given in Table 3 [55-56]:

$$E = 0.5 \, C_{sp} \, (\Delta V)^2 \tag{3}$$

$$P = E/t \tag{4}$$

where C_{sp} is the specific capacitance of the supercapacitor (F g^{-1}), ΔV is the voltage change during the discharge process after IR drop in V and t (h) is the time for a sweep segment. Table 3 shows that both CuCo$_2$O$_4$, and MnCo$_2$O$_4$, have a high energy density of 325 Wh Kg^{-1} and 242 Wh Kg^{-1} at a power density equal to 89 WK g^{-1} and 97 WK g^{-1}, respectively. It's clarified that the nanocomposites CuCo$_2$O$_4$ and MnCo$_2$O$_4$ exhibit a high-quality electrochemical reversibility and signifies the highest energy and superior stability as well as the highest specific capacitance values of 915 and 690 F g^{-1}.

Table 3. The energy density and power density of the investigated samples
at current density 56 mA g^{-1}.

Sample	E_d (WhK g^{-1})	P_d (WK g^{-1})
CuCo$_2$O$_4$	325	89
NiCo$_2$O$_4$	139	89
MnCo$_2$O$_4$	242	97
MnNiCo$_2$O$_4$	52	97
CuMnCo$_2$O$_4$	101	94
CuNiCo$_2$O$_4$	48	93

The electrochemical properties of the studied samples were further assessed with electrochemical impedance spectroscopy (EIS). The EIS were examined to not only affirming the above results obtained via CVs and charge-discharges but also to obtain information relating to the facile transport of ions and electrons and their conductivities. The EIS was performed at an open potential over the frequency margin of 0.1-100 kHz with amplitude equal to 5 mV and given in Fig. 11.

The Nyquist plots indicate precise semicircles at high frequencies for all nanocomposites and linear part at low frequencies. The semicircle is related to the charge transfer resistance of the

electrode, which is ascribed to the faradaic redox reaction. The charge-transfer resistances R_{ct} can be evaluated from the diameter of this semicircle and presented in Table 2. R_{ct} was found to decrease in the order: $CuCo_2O_4 < MnCo_2O_4 < NiCo_2O_4 < CuMnCo_2O_4 < MnNiCo_2O_4 < CuNiCo_2O_4$. The low values of R_s and R_{ct} of both $CuCo_2O_4$ and $MnCo_2O_4$ are indicating that they have the least interfacial charge-transfer resistance and lowest diffusion resistances and thus revealed the highest specific capacitance, compared to rest of nanocomposites.
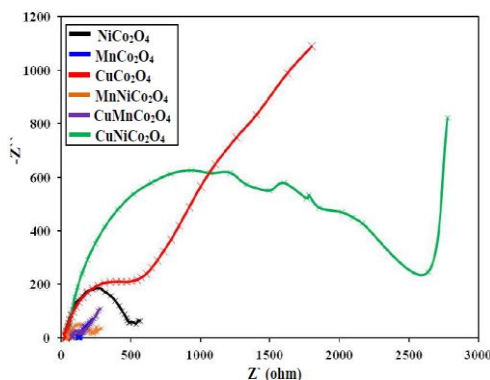

Fig. 11. Nyquist impedance spectra of all studied samples.

4. Conclusion

A simple route for fabrication ternary oxides ($NiCo_2O_4$, $CuCo_2O_4$, $MnCo_2O_4$) and quaternary mixed oxides ($CuNiCo_2O_4$, $CuMnCo_2O_4$, $MnNiCo_2O_4$) having a spinel structure via a urea and surfactant-assisted co-precipitation method. High respect ratio rods and spheres are obtained for all samples with a mesoporous structure. $CuCo_2O_4$ samples consist of CuO and $CuCo_2O_4$ spinel structure and $MnCo_2O_4$ consisted of MnO_2 and $MnCo_2O_4$ spinels structure which give them a good electrochemical performance when used as a supercapacitor electrode material. $CuCo_2O_4$ and $MnCo_2O_4$ have a large capacitance of 915 F g^{-1} and 690 F g^{-1}, respectively; at 56 mA g^{-1}. The quaternary oxides have comparatively low electrochemical performance. Both $CuCo_2O_4$ and $MnCo_2O_4$ electrodes show capacitance retention of 99 and 97.8 %, respectively which explain their superior cycle stability.

References

[1] A. S. Arico, P. Bruce, B. Scrosati, J. M. Tarascon, W. VanSchalkwijk, Nat. Mater. **4**, 366 (2005).
[2] X. Huang, Z. Zhang, B. Song, Y. Deng, S. Liu, Y. Cui, G. Wang, C. P. Wong, J. Alloy. Compd. **656**, 663 (2016).
[3] Y. Xu, L. Wang, P. Cao, C. Cai, Y. Fu, X. Ma, J. Power Sources **306**, 742 (2016).
[4] C. Liu, F. Li, L.P. Ma, H. M. Cheng, Adv. Mater. **22**, 28 (2010).
[5] X. F. Wang, X. H. Lu, B. Liu, D. Chen, Y. X. Tong, Adv. Mater. **26**, 4763 (2014).
[6] D. Bruce, K. Haresh, T. Jean-Marie, Science **334**, 928 (2011).
[7] D. Sarkar, G. G. Khan, A. K. Singh, K. Mandal, J. Phys. Chem. C **117**, 15523 (2013).
[8] R. Arunachalam, R. M. Gnanamuthu, M. Al Ahmad, S. Mohan, R. Pavul Raj, J. Maharaja,

N. Al Taradeh, A. Al-Hinai, Surf. Coat. Technol. **276**, 336 (2015).

[9] A. K. Ramasami, M. V. Reddy, G. R. Balakrishna, Mater. Sci. Semiconduc. Proc. **40**, 194 (2015).

[10] V. Aravindan, M. V. Reddy, S. Madhavi, G. V. S. Rao, B. V. R. Chowdari, Nanosci. Nanotechnol. Lett. **4**, 724 (2012).

[11] M.V. Reddy, Z. Beichen, K. P. Loh, B. V. R. Chowdari, Cryst. Eng. Comm. **15**, 3568 (2013).

[12] W. Sun, X. Rui, M. Ulaganathan, S. Madhavi, Q. Yan, J. Power Sources **295**, 323 (2015).

[13] C. Chen, M. Cho, Y. Lee, J. Mater. Sci. **50**, 6491 (2015).

[14] W. Li, K. Xu, G. Song, X. Zhou, R. Zou, J. Yang, Z. Chen, J. Hu, Cryst. Eng. Comm. **16**, 2335 (2014).

[15] D. Zhang, H. Yan, Y. Lu, K. Qiu, C. Wang, Y. Zhang, X. Liu, J. Luo, Y. Luo, Dalton Trans. **43**, 15887 (2014).

[16] L. Li, Y. Q. Zhang, X. Y. Liu, S. J. Shi, X. Y. Zhao, H. Zhang, X. Ge, G. F. Cai, C. D. Gu, X. L. Wang, J. P. Tu, Electrochim. Acta **116**, 467 (2014).

[17] S. G. Krishnan, M. V. Reddy, M. Harilal, B. Vidyadharan, I. I. Misnon, M. H. A. Rahim, J. Ismail, R. Jose, Electrochim. Acta **161**, 312 (2015).

[18] Y. Xu, X. Wang, C. An, Y. Wang, L. Jiao, H. Yuan, J. Mater. Chem. A **2**, 16480 (2014).

[19] A. Pendashteh, M. S. Rahmanifar, R. B. Kaner, M. F. Mousavi, Chem. Commun. **50**, 1972 (2014).

[20] M. Zhu, D. Meng, C. Wang, G. Diao, ACS Appl. Mater. Interf. **5**, 6030 (2013).

[21] R. K. Selvan, O. Augustin, L. J. Berchmans, R. Saraswathi, Mater. Res. Bull. **38**, 41 (2003).

[22] H. P. Klug, L. E. Alexander, X-ray diffraction procedures, Wiley, New York, (1970).

[23] H. S. Jadhav, A. K. Rai, J. Y. Lee, J. Kim, C.-J. Park, Electrochim. Acta **146** 270 (2014).

[24] C.-Y. Cao, J. Qu, W.-S. Yan, J.-F. Zhu, Z.-Y. Wu, W.-G. Song, Langmuir **28**, 4573 (2012).

[25] T. Yousefi, R. Davarkhah, A. N. Golikand, M. H. Mashhadizadeh, Mater.Sci. Semiconduct. Proc. **16**, 868 (2013).

[26] J. Du, Y.Pan, T. Zhang, X. Han, F. Cheng, J. Chen, J. Mater. Chem. **22**, 15812 (2012).

[27] J. Tang, A. P. Alivisatos, Nano lett. **6**, 2701 (2006).

[28] C. T. Sun, D. F. Xue, Cryst. Eng. Comm. **16**, 2129 (2014).

[29] C. T. Sun, D. F. Xue, Cryst. Growth Des. **14**, 2282 (2014).

[30] M. A. Mousa, W. A. A. Bayoumy, M. Khairy, Mater. Res. Bull. **48**, 4576 (2013).

[31] M. M. Mohamed, M. Khairy, S. Eid, Electrochim. Acta **263**, 286 (2018).

[32] M. M. Mohamed, S. M. A. Katib, Appl. Catal. Gen. **287**, 236 (2005).

[33] E. I. Ross-Medgaarden, I. E. Wachs, J. Phys. Chem. C **111**, 15089 (2007).

[34] M. M. Mohamed, M. Khairy, Salah Eid, Electrochim. Acta **263**, 286 (2018).

[35] B. Lefez, P. Nkeng, J. Lopitaux, G. Poillerat, Mater. Res. Bull. **31**, 1263 (1996)

[36] X.-H. Xia, J.-P. Tu, Y.-Q. Zhang, Y.-J. Mai, X.-L. Wang, C.-D. Gu, X.-B. Zhao, RSC Adv. **2**, 1835 (2012).

[37] V. D. Patake, C. D. Lokhande, O. S. Joo, Appl. Surf. Sci. **255**, 4192 (2009).

[38] M. Aghazadeh, J. Appl. Electrochem. **42**, 89 (2012).

[39] Q. Li, L. Zeng, J. Wang, D. Tang, B. Liu, G. Chen, M. Wei, ACS Appl. Mater. Interf. **3**, 1366 (2011).

[40] S. G. Hwang, S. H. Ryu, S. R. Yun, J. M. Ko, K. M. Kim, K. S. Ryu, Mater. Chem. Phys. **130**, 507 (2011).

[41] S. Verma, H. M. Joshi, T. Jagadale, A. Chawla, R. Chandra, S. Ogale, J. Phys. Chem. C **112**, 15106 (2008).

[42] Y. Li, X. Houa, Z. Zhanga, Z. Haib, H. Xuc, D. Cuia, S. Zhuiykovb, C. Xuea, Appl. Surf. Sci. **436**, 242 (2018).

[43] I. Nikolov, R. Darkaoui, E. Zhecheva, R. Stoyanova, N.Dimitrov, T. Vitanov, J. Electroanal. Chem. **429**, 157 (1997).

[44] R. N. Singh. H. Hamdani, J. F. Koenig, G. Pollierat, J. L. Gautier, P. Chartier, J. Appl. Electrochem. **20**, 442 (1990).

[45] A. J. Bard, R. Parsons, J. Jordan (Eds.), M. Dekkar, Standard Potentials in Aqueous Solutions, New York, (1985).

[46] G. M. Thorat, H. S. Jadhav, J. G. Seo, Ceramics Intern. **43**, 2670 (2017).

[47] Y. Xu, X. Wang, C. An, Y. Wang, L. Jiao, H. Yuan, J. Mater. Chem. A **2**, 16480 (2014).

[48] A. K. Singh, D. Sarkar, K. Karmakar, K. Mandal, G. G. Khan, ACS Appl. Mater. Interfaces **8**, 20786 (2016).

[49] X. Lu, M. Yu, T. Zhai, G. Wang, S. Xie, T. Liu, C. Liang, Y. Tong, Y. Li, Nano Lett. **13**, 2628 (2013).

[50] A. Ramadoss, B. Saravanakumar, S. J. Kim, Nano Energy **15**, 587 (2015).

[51] D. Qu, J. Power Sources **109**(2), 403 (2002).

[52] Y. Jiao, Y. Liu, B. S. Yin, S. W. Zhang, F. Y. Qu, X. Wu, Nano Energy **10**, 90 (2014).

[53] F. He, K. Liu, J. Zhong, S. Zhang, Q. Huang, C. Chen, J. Electroanal. Chem. **749**, 89 (2015).

[54] M. Lee, S. K. Balasingam, H. Y. Jeong, W. G. Hong, H. B. Lee, B. H. Kim, Y. Jun, Sci. Reports **5**, 8151 (2015).

[55] M. A. Mousa, M. Khairy, M. Shehab, J. Solid State Electrochem. **21**, 995 (2017).

[56] J. Zhu, M. Chen, H. Qu, Z. Luo, S. Wu, H. A. Colorado, S. Wei, Z. Guo, Energy Environ. Sci. **6**, 194 (2013).